Next Materials 7 (2025) 100524

Contents lists available at ScienceDirect

Next Materials

journal homepage: www.sciencedirect.com/journal/next-materials

Research article

Forming ability of the WC-based ceramic metal composites with different Fe-based binders by unique laser beam modulation

H.S. Maurya [a,b,*], K. Juhani [a], F. Sergejev [a], R. Kumar [a,c], A. Hussain [a], K.G. Prashanth [a,d]

[a] *Department of Mechanical and Industrial Engineering, Tallinn University of Technology, Ehitajate tee 5, Tallinn 19086, Estonia*
[b] *Department of Engineering Sciences and Mathematics, Luleå University of Technology, Luleå SE 97187, Sweden*
[c] *Laboratory for Tribology and Interface Nanotechnology, Faculty of Mechanical Engineering, University of Ljubljana, Bogišićeva 8, Ljubljana 1000, Slovenia*
[d] *CBCMT, School of Mechanical Engineering, Vellore Institute of Technology, Vellore, Tamil Nadu 630014, India*

ARTICLE INFO

Keywords:
WC-based composites
SLM
Laser beam modulation
Microstructure
Crack mitigation

ABSTRACT

Additive manufacturing enables the production of cermet parts encompassing intricate geometries and tailored microstructures. The present study investigates the fabrication of WC-based Ceramic metal composites (CMC) with pure Fe and ferritic stainless steel (AISI Grade 430 L) green binders by controlling melt pool temperature during the Selective laser melting process. A study of crack restraining and formability of WC composite parts with different Fe-based binder compositions has been conducted by adapting Laser beam modulation (LBM). As a result of optimizing the laser beam with variations in laser power peaks (48, 60, and 72 Watt) and constant exposure times for each laser beam profile, the melt pool temperature was regulated, primary cracks in the parts were reduced and this resulted in the fabrication of the parts with reduced process defects such as internal thermal cracks. The reduction in cracks has been attributed to a lower thermal gradient, which has affected the microstructure and microhardness of the as-built parts. Scanning electron microscope (SEM) and X-ray diffraction (XRD) analysis have been used to study the microstructure and phase formation in the fabricated parts. The maximum microhardness (2048 ± 209 HV_1) has been achieved for the fabricated cermets parts with ferritic stainless steel binder with the composition of WC-20 wt% FeCr.

1. Introduction

Cemented carbides (WC-Co) are considered an excellent machine tool material due to impeccable mechanical and tribological properties including a superior hardness-toughness balance, abrasion and chemical resistance, thermal shock resistance, and high softening temperatures that lead to decent high-temperature stability [1,2]. High-end wear-resistant cemented carbide parts are widely utilized in deep-drilling, machining of superalloy or difficult-to-machine materials, high-speed dry-cutting, or the areas of severe cyclic mechanical-thermal encounters [3,4]. However, a major limitation in its fabrication lies in the use of the binder metal "Co", which is not only a crucial rare metal, but also its geopolitical supply is a major concern [5–7]. A substitute binder metal that can replace Co is Ni, which shares similar chemical and physical properties. Besides, both binder metal shows better wettability and can greatly improve the mechanical properties of cemented carbide [8,9]. Nonetheless, recently, both Ni and Co have been declared carcinogens to human health by several agencies including the European REACH (Registration, Evaluation, Authorization, and Restriction of Chemical Substances) program and the U.S. National Toxicology Program, and their use is strictly to be minimized [10,11]. This has led to the search for an alternative that is less toxic, easily available, low-cost, recyclable, and that could partially or completely substitute Ni and Co without compromising the mechanical properties of cemented carbides [12,13].

In this regard, our previous studies have shown that Fe-based alloys could act as a potential greener binder alternative to Ni/Co towards powder metallurgy of tungsten carbide-based composite [9,14]. It was reported that Fe-based alloys with Cr content act as a growth inhibitor in WC-based carbide and exhibit lower rupture strength as compared to traditional WC-Co/Ni-based cermet [7]. Moreover, it was reported that different Fe-based alloys can be used to tailor the cermet parts with different phase structures (austenitic/ferritic/martensite), which can further be utilized to tailor the mechanical and tribological properties while also enhancing the oxidation and corrosion resistance of the cermet parts.

Selective laser melting (SLM)/ laser powder bed fusion (LPBF) is a

---

[*] Corresponding author at: Department of Mechanical and Industrial Engineering, Tallinn University of Technology, Ehitajate tee 5, Tallinn 19086, Estonia
E-mail addresses: himanshu.singh.maurya@associated.ltu.se, himanshudes@gmail.com (H.S. Maurya).

https://doi.org/10.1016/j.nxmate.2025.100524
Received 11 June 2024; Received in revised form 27 January 2025; Accepted 5 February 2025

one-step additive manufacturing (AM) technology in which coherent high-intensity laser energy is focused on the powder bed to melt and fuse the powder particles to fabricate the final parts [15,16]. Fabrication of the WC-based cermets via the conventional powder metallurgical route has some limitations/disadvantages such as the complexity of the produced parts, increasing post-processing steps, grain coarsening due to longer sintering times, and formation of the brittle phase due to decarburization, etc. [15,17]. These disadvantages can be overcome by employing AM methods such as SLM/LPBF. Due to its unique solidification technique by laser exposure, the as-built parts exhibit a variation in microstructure and mechanical properties [18,19]. Nevertheless, fabrication of the cermets parts via SLM/LPBF is still challenging due to its inherent brittleness, which leads to the formation of cracks during the solidification process [20–23]. Besides, the SLM process exhibits rapid solidification rates in the order of 10^{11}-10^{15} K/s [24,25], which results in high thermal gradients in the melt pool, generates higher thermal residual stresses in the parts [26–28], and introduces process defects such as cracks and porosity in the as-built parts [29–31]. The coefficient of thermal expansion (CTE) of the matrix and binder during the thermal cycle by laser exposure is a source for the generation of the residual stress that results from non-uniform expansion and contraction, especially in the case of CMCs, studies on which are rare. To this end, current work reports on additive manufacturing of WC-based composites and more precisely on the micro-mechanics of formability of the WC-based cermets in conjunction with Fe-base binders without the presence of cracks.

Accordingly, in this study, a unique laser beam modulation (LBM) technique has been adapted to control the melt pool temperature by varying the laser peaks with different laser exposure times at the same exposure point that may be used for preheating/cooling the powder bed during the fabrication process which, ultimately helps to lower the thermal gradient and reduces the residual stress and help to achieve crack-free parts. As per the author's best knowledge, no research has been carried out on the fabrication of the WC-FeCr-based cermets by the SLM process. Research based on the WC-Fe/Ni-based composites has been performed by different laser-based fabrication processes such as laser cladding and DED to study the crack mitigation in the parts [6,32,33]. In this work, Fe and Fe-based alloys have been used as a green binder system with different weight percentages to investigate the effect on the formability of the WC as-built parts by the laser beam optimization and its effect on their mechanical properties thereof.

2. Materials and method

2.1. Powder preparation

The feedstock powder mixture (WC and FeCr) has been prepared in a mechanical mixer for 24 h at 20 rpm. Yttria-stabilized zirconia (YSZ) balls were used. The composition and sample designation of the as-built parts are depicted in Table 1. Initial WC powder (provided by Pacific Particulate Materials Ltd.) has a nearly spherical morphology with a particle size of <10 μm while pure Fe (supplied by TLS Technik GmbH) and 430 L ferritic stainless steel (supplied by Sandvik osprey Ltd.) has a particle size ranging between 10 and 45 μm with spherical morphology.

Table 1
Sample designation and composition of the different ceramic metal composites fabricated using the selective laser melting process in the present study.

Sample designation	WC (wt%)	Fe (wt%)	Cr (wt%)
WC−50Fe (WC + 50 % Fe)	50	50	NIL
WC−50FeCr (WC + 50 % 430 L)	50	41.60	8.40
WC−20FeCr (WC + 20 % 430 L)	80	16.64	3.36

2.2. SLM fabrication

An SLM realizer 50 equipped with an Nd: YAG pulsed laser with a maximum power of 100 W was employed to fabricate the cermet parts. A stainless-steel substrate was used and an argon atmosphere to avoid the oxidation of the melt pool during the fabrication. Different laser process parameters have been used to fabricate the cuboidal parts with a dimension of 2 × 2 × 4 mm^3. Laser beam modulation (LBM) has been used to fabricate the cermet parts and to study the effect of crack mitigation on the fabricated cermets. A point scan strategy has been used as the hatch style. Schematics of the laser beam modulation with multiple laser peaks within the single laser profile has been depicted in Fig. 2. During the LBM process the adapted laser beam consisting of multiple laser peaks with different laser power/energy densities and exposure times was exposed to a single exposure point and are repeated to each exposure point with the same parameters to control the melt pool temperature (Fig. 2). Laser peaks with low energy density (preheat the powder bed (PH1 and PH2)) have been used followed by laser peaks with higher energy density (MLP) to melt and fuse the powder particle. This is followed again by laser peaks with low energy density with extended laser exposure time to control the cooling of the melt pool (CL1 and CL2). In all the cases only MLP has been varied (48, 60, and 72 W) to study the effect of the process parameters on the fabrication of the cermets parts. All other parameters were kept constant. The different laser process parameters used for the fabrication of the CMC parts have been depicted in Table 2.

2.3. Microstructure and mechanical characterization

For the microstructural and phase analysis, Zeiss FEG scanning electron microscope (SEM) and Rigaku Smart lab, X-ray diffractometer (XRD) were used respectively. Specimens for the analysis were prepared by mounting, grinding, and polishing according to standard hard metal procedures. For the microhardness test (ASTM E384–17), Vickers Micromet 2001 was used at room temperature to obtain the microhardness of the as-built CMC parts at 1 kg load with a dwell time of 10 seconds. Porosity was determined using the image analysis software Image J (version 1.53e). Measurements of five different areas at magnification 250 times per batch have been analyzed and the average value has been reported. Micrographs of the as-built samples taken at various magnifications using the optical microscope were used for the porosity analysis. All the analysis was conducted 3 times for the reliability and reproducibility of the results.

3. Result and discussion

3.1. Microstructure

Fig. 3 exhibits the SEM micrograph of the WC-50Fe cermets fabricated as a function of varying laser power. The low magnification microstructure (Fig. 3(a,d,g)) shows the presence of a typical laser track morphology along with some cracks and pores present in these cermets. In addition, bimodal microstructures (with the presence of fine and coarse WC grains) with heterogeneous distribution can be seen in all three samples (Fig. 3(b,e,h)), which can be attributed due to the presence of a Gaussian laser energy distribution [18,34]. The fine WC particles show equiaxed/dendritic morphologies. Due to the Gaussian distribution of the laser beam, the laser energy is concentrated more at the center of the laser focal point and gradually decreases towards the edges [35]. This variation in the laser energy distribution led to the formation of a gradient microstructure in the WC cermets. The thermal gradient and solidification rate are two important factors contributing to the formation of WC with different morphologies. The formation of the η-phase cannot be observed in the WC-50Fe composites; only two phases WC (bright phase) and Fe-Cr-based binder (dark phase) are observed.

Increasing the laser energy leads to the formation of an elongated/

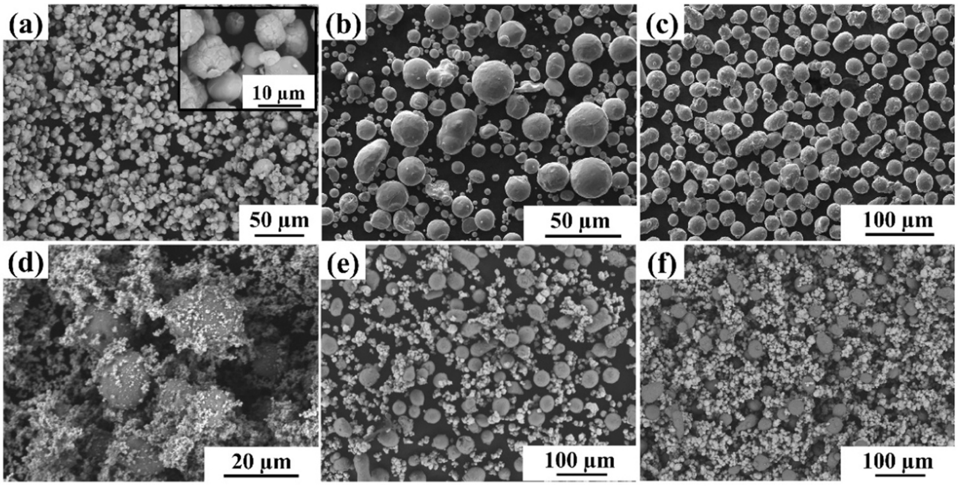

Fig. 1. Scanning electron micrographs of the initial powder feedstock: (a) WC; (b) Fe; and (c) 430 L Stainless steel, and scanning electron micrography images of the mixed feedstock powder (d) WC-50 wt%Fe (WC-50Fe); (e) WC-50 wt% 430 L stainless steel (WC-50FeCr); and (g) WC-20 wt% 430 L stainless steel (WC-20FeCr).

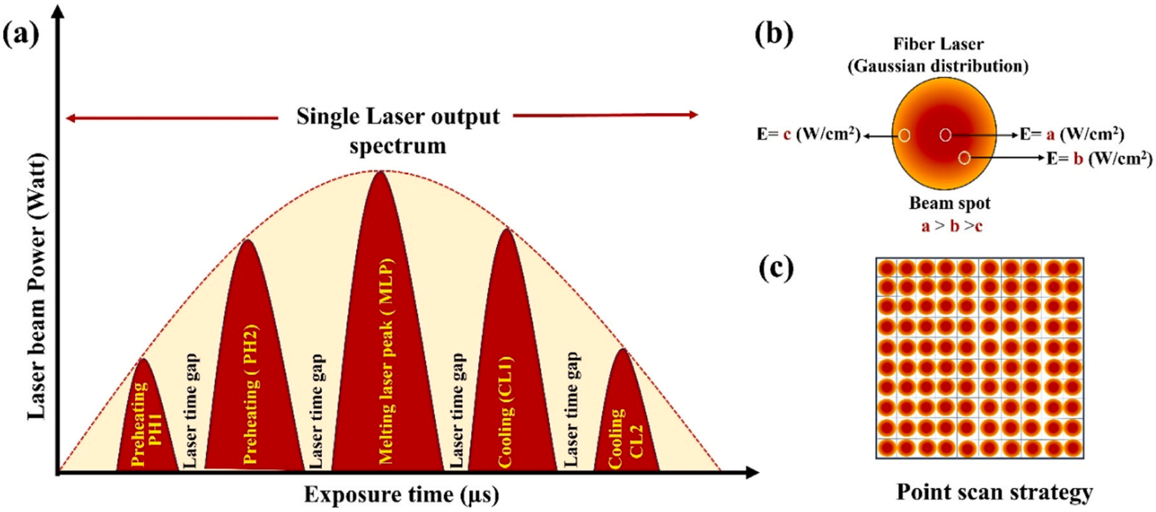

Fig. 2. Schematics illustrating (a) Single laser beam profile consisting of Preheating laser peaks (PH1 and PH2), Laser melting peak (LMP), and cooling peaks (CL1 and CL2); (b) Gaussian laser energy distribution; (c) Point scanning strategy adapted for the laser scan.

Table 2
Laser process parameters adapted for the fabrication of the WC-Fe-based cermets.

Sample designation	**Exposure time** (µs)	**Laser power (Watt)** PH1-PH2-LMP-CL1-CL2	**Hatch distance** (mm)	**Layer** thickness (mm)
WC−50Fe−1	100–200–200–500–200	12–24–48–19.2–14.4	0.045	0.035
WC−50Fe−2		12–24–60–19.2–14.4		
WC−50Fe−3		12–24–72–19.2–14.4		
WC−50FeCr−1		12–24–48–19.2–14.4		
WC−50FeCr−2		12–24–60–19.2–14.4		
WC−50FeCr−3		12–24–72–19.2–14.4		
WC−20FeCr −1		12–24–48–19.2–14.4		
WC−20FeCr −2		12–24–60–19.2–14.4		
WC−20FeCr −3		12–24–72–19.2–14.4		

dendritic WC phase due to relatively higher cooling rates. However, at higher laser power (72 W), grain coarsening can be observed, which may be attributed to an increased melt pool temperature. The laser Gaussian distribution of energy results in a temperature gradient (G) with a higher value at the center of the melt pool and a lower value at the boundaries [36]. The variation in the microstructural formation (dendritic and coarser) of the SLM-processed composite parts is influenced by their thermal gradient (G), solidification rate (R), and melt pool cooling rate ($T = G \times R$), where G is the temperature gradient over a distance and varies according to place and time in the melt pool and R depends on the scan speed of the laser and scanning angle [37,38]. Fineness of the microstructure formation is determined by the cooling rate of the melt pool ($G \times R$). In general, a higher cooling rate leads to finer microstructures in materials [39,40]. As an advantage of the SLM process, high cooling rates are achieved in the order of 10^3 and 10^{11}K/s, which results in fine microstructures in the SLM-processed parts at

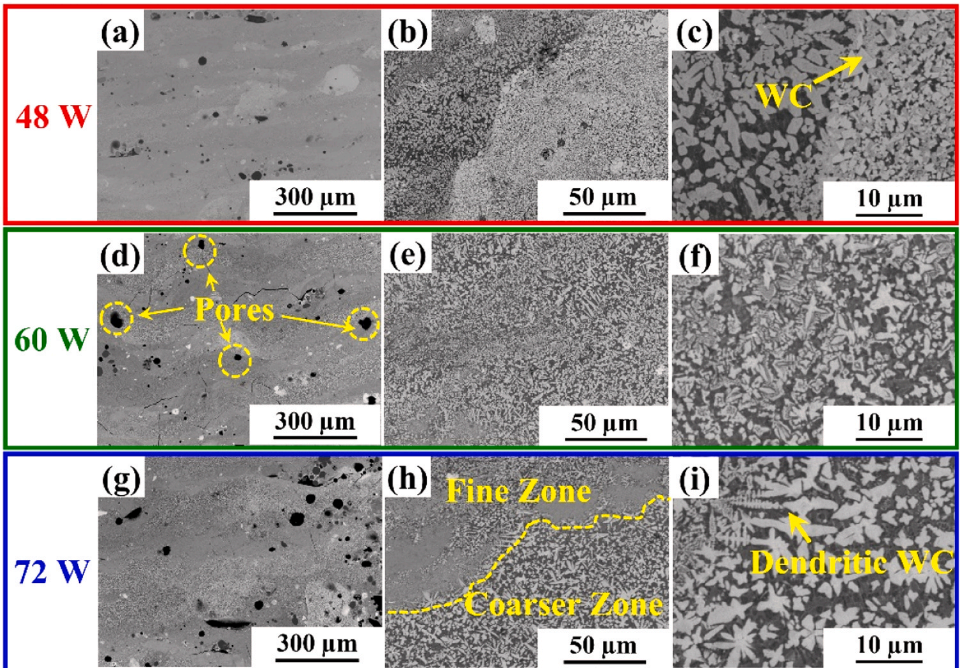

Fig. 3. Scanning electron microstructures of the WC-50Fe-based composites fabricated as a function of different laser power.

higher laser peak power [41,42]. However, a high laser energy density has an adverse effect on the cooling rate of the melt pool as it raises the overall powder bed's temperature, and thus high laser peak power results in reduced cooling rates and leads to coarsening of the carbide phases. Based on the Gaussian distribution of laser energy, the melt pool maximum temperature is proportional to $P/\sqrt{v}$ ratio [43]:

$$T_{\max} \propto \frac{P}{\sqrt{v}} \tag{1}$$

where P corresponds to the laser power, and v denotes the scanning speed.

At lower laser peak power (48 W), lower temperatures are achievable in the melt pool, resulting in lower G, and thus, smaller G/R. A smaller G/R ratio results in more equiaxed grains. Increasing the laser melting peak power (60 W) led to a fine dendritic carbide morphology with a lower gradient size in the WC phases (dendritic and coarser). This may be attributed to an increment in the laser energy density and thus increases the temperature of the melt pool, affecting the sample's heating/cooling rate. The cooling rate increases with MLP energy density. However, further increasing the laser's power resulted in the coarsening of the microstructure (72 W). The high energy of the laser beam, which results in variation in the cooling rate and non-equilibrium circumstances during solidification, may be responsible for such microstructural characteristics. In conclusion, these microstructures of

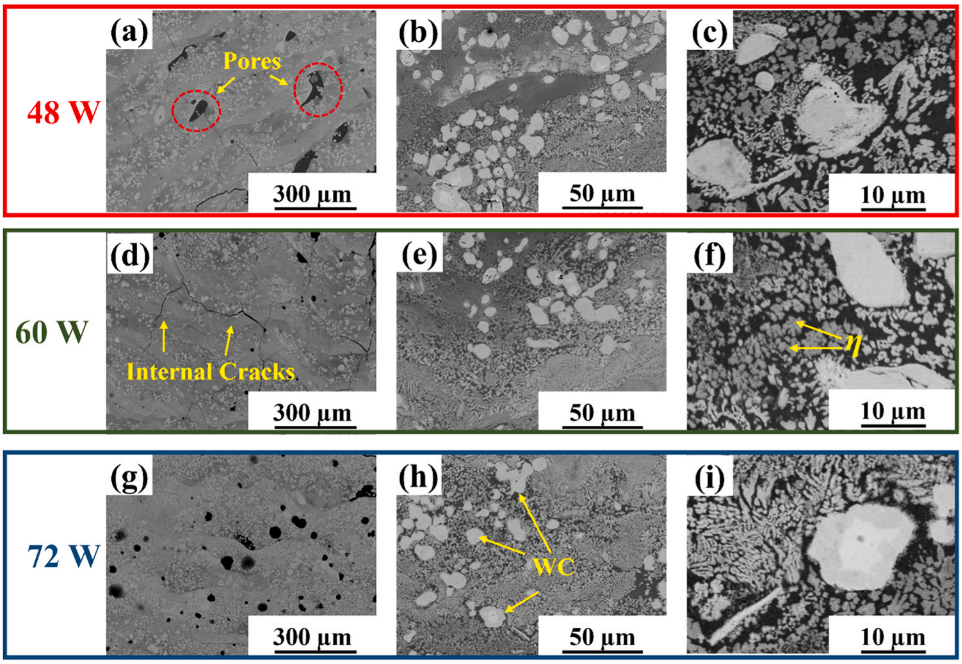

Fig. 4. Scanning electron microscopy images of the WC-50FeCr-based cermets fabricated as a function of different laser power.

the as-built parts are highly dependent on both the laser peak power and laser scanning speed, and thus, a change in these parameters may significantly influence the microstructural formation and in turn, their mechanical properties of the SLM fabricated parts.

The microstructure of the WC-50FeCr cermets fabricated as a function of varying laser parameters is depicted in Fig. 4. Unlike the WC-50Fe samples, the SEM microstructures of WC-50FeCr cermets show the presence of three different phases: dark binder phase, bright WC phase, and grey η-phase. The presence of heterogeneity in the phase distribution can be observed due to the Gaussian laser energy distribution. The η-phase is observed in the WC-50FeCr cermets irrespective of the laser power used. However, using a lower power of 48 W formation of these complex carbides is more distinct, and an increase in the laser energy density could lead to the dissolving of the complex intermetallic carbide partially and reduction volumetrically.

Fig. 5. exhibits the microstructure of the WC-20FeCr composites fabricated at different laser energy densities. The morphology of the phases in the microstructure is different from the WC-Co-based cermets fabricated by SLM. Two different morphologies of the carbide phases can be observed in all the microstructures with fine and coarse equiaxed particles. The dark region corresponds to the binder phase with Fe-Cr while the bright region quadrates to the WC phase. The lower number of intermetallic phases (η- phase or metal complex carbide) can be observed in the microstructures that could be attributed to the lower volumetric percentage of the binder phase based on the Fe-Cr. Moreover, a coarser WC phase can be observed, and increasing the laser energy density results in the coarsening of the microstructure. The coarsening of the microstructure can be explained by the increment in the melt pool temperature by increment in the laser powder and lower the cooling rate. Changes in cooling rate and increment in the melt pool temperature led to the coarsening of the microstructure during solidification. The cooling/solidification rate plays an important role in the formation of the microstructure shape and fineness as explained earlier.

Fig. 6 depicts the elemental mapping of the WC-based cermets with different compositions of the binders. For the WC-50Fe cermet, the W distribution is quite homogenous and corroborates with the SEM micrograph. However, Fe and C distribution can be observed in the W and the binder phases which suggest the formation of the intermetallic carbide phases. In the case of the cermet with ferritic stainless steel as the binder, some WC-rich phases can be observed with the formation of the binder intermetallic carbide phases. In both cases, the interaction and formation of the carbide of the binder elements with the WC can be observed.

3.2. Crack mitigation

Cermets are a highly brittle material that is susceptible to crack formation during SLM fabrication. SLM's rapid solidification process led to the formation of these cracks in the parts and affected the formability and mechanical properties of the parts. Parts with a single laser scan without a laser beam optimization have rapid heating/cooling rates that can lead to generating higher thermal residual stress in the parts as explained earlier and lead to the failure of the parts fabrication due to a large number of cracks in the parts. Samples were attempted to fabricate without LBM before optimizing the laser beam but were unable to fabricate due to large thermal gradients and residual stress generation in the parts, which affected the fabrication process. By controlling the melt pool temperature and reducing the sudden heating/cooling rate, the fabrication of the parts was successful with no major primary cracks in the as-built parts. However, it can be observed from (Figs. 3, 4, and 5(a, d, g)) that minor cracks are visible in the parts which could be due to laser process parameters and differences in the thermal expansion coefficient of the matrix and binder phase. LBM helps to reduce the major cracks in the final parts and can produce parts but complete elimination of the cracks in the parts cannot be achieved.

It can be concluded that controlling the powder bed temperature and reducing the heating and cooling rate could lead to the production of dense parts in the future. However various factors must be included such as powder morphology, substrate preheating, and double melting may be able to help further reduce the cracks. Binder material composition also plays an important role in the fabrication of the parts. As a result of laser deposition, FeCr alloys such as AISI 430 L are fracture-sensitive and exhibit microstructures comprised of brittle martensite as well as retained austenite [44]. The content of the hard phase in the powder batch plays a decisive role in generating hot cracks during SLM processing. These hard phases are brittle in nature and lead to thermal cracks during SLM processing due to high thermal residual stress and the complex history of the process. The cracking sensitivity of the

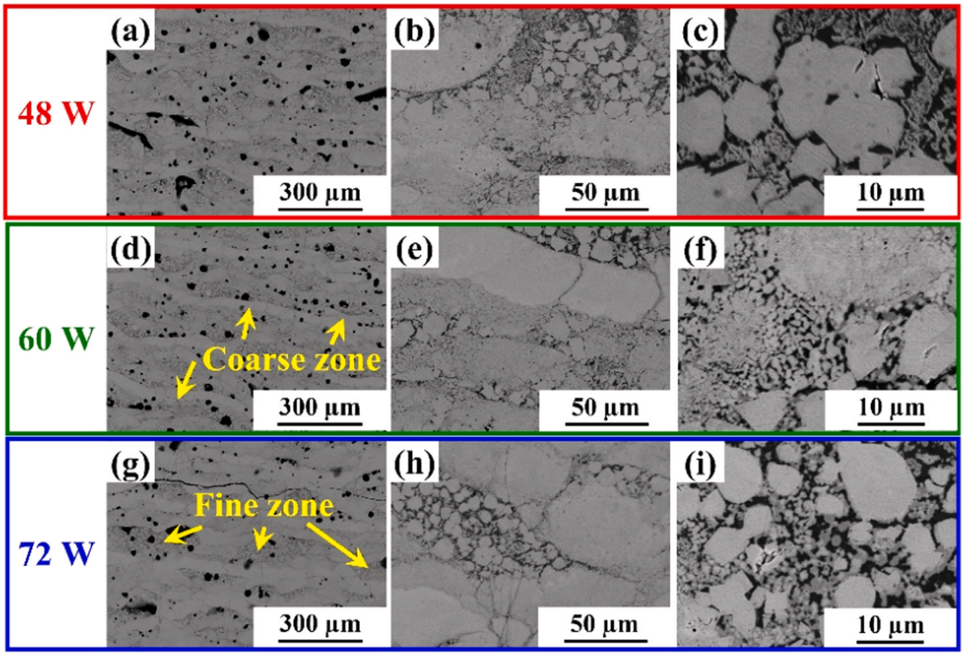

Fig. 5. SEM micrograph of the WC-20FeCr based cermet with different laser power.

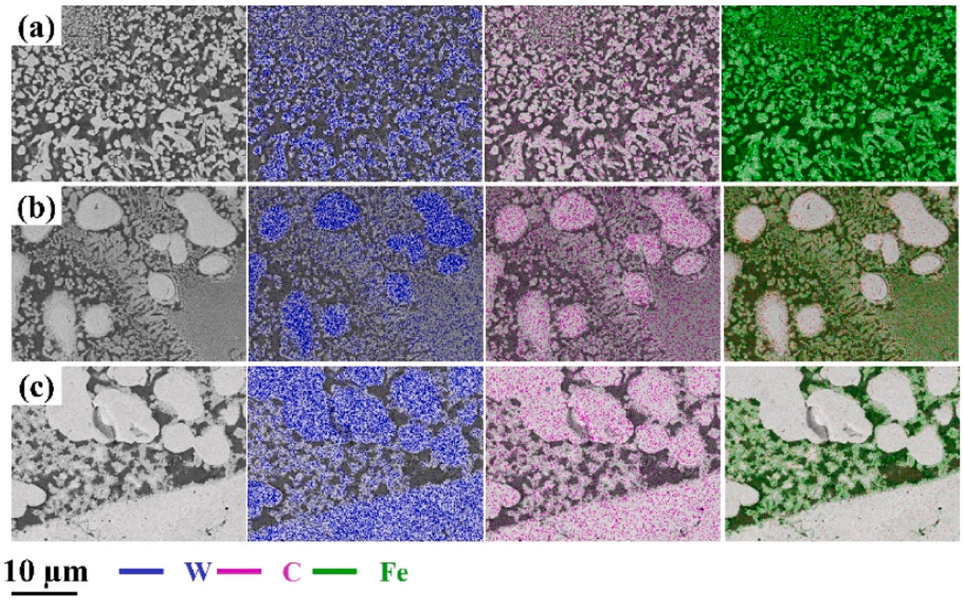

Fig. 6. EDS mapping of the WC-based cermet with 60-watt laser power (a) WC-50Fe, (b) WC-50FeCr, (c) WC-20FeCr.

composites increases with the increment of the WC phase content in hard metals. Moreover, binder elements also play a significant role as both Fe (Iron) and Cr (Chromium) have the affinity to form carbides, particularly at high temperatures [45]. The type of carbide formed can depend on the specific alloy and its composition. In particular, chromium exhibits a stronger carbon affinity than iron. This means that when chromium is present in a steel alloy, it tends to form more carbides with carbon, which can contribute to the formation of Cr-rich carbides such as M_7C_3 and $M_{23}C_6$ [46,47]. The use of the FeCr-based binder with the WC led to the formation of complex intermetallic carbide may lead to cracking and reduced high-temperature plasticity.

3.3. Effect on the hardness

Fig. 7. exhibits the microhardness variation of the composite parts with different laser power. It can be observed that the microhardness value increases with an increment in the laser power in all the cases which can be attributed to the fineness of the WC phase and the formation of the intermetallic carbide phases in the binder. However, in the case of WC-50Fe, a different trend can be observed due to the effect of the coarsening of the grain and the increment in the porosity. Large variation in the hardness value can be observed in the as-built part which can be explained by the non-homogeneous phase distribution and different WC phase sizes. The variation in the hardness value can also depend on the indenter placed area. The indenter covering the area with binder-rich phases exhibits a lower hardness value due to its soft phase while if the indenter is placed in the fine area of the WC carbide phase the diagonal of the indenter is not deep due to the high hardness value of the WC phases (Fig. 8). In addition, the unwanted η- phase affects the microhardness and toughness due to the reduction of the carbon content and promotes the cracking in the parts. The maximum hardness was achieved for WC-20FeCr which could be due to a higher carbide percentage and larger WC particle (Fig. 8(c)). WC with pure Fe binder exhibits poor wettability during solidification which leads to affecting mechanical properties of the fabricated parts. The inclusion of Cr in the binder could be beneficial as it leads to retard the carbide grain growth and improve the mechanical properties [48]. During SLM processing of the Fe–Cr based alloy powder, many carbide strengthening phases such as M_7C_3, and $M_{23}C$ where M= Fe, Cr, were produced, which may contribute to improved wear resistance and hardness of the material

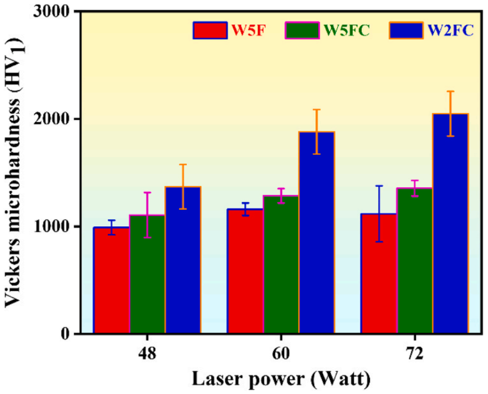

Fig. 7. Microhardness of the WC-based composites with variation in the laser process parameters.

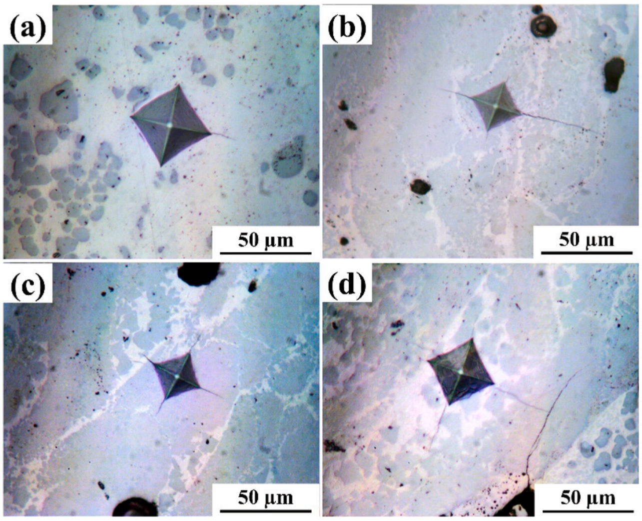

Fig. 8. An optical microscope image of the Vickers microhardness of the WC-based composites exhibits the variation in the length of the diagonal due to the bimodal grain distribution of the WC (a) WC-50Fe, (b)WC-50FeCr, (c, d) WC-20FeCr.

[49]. Moreover, high content of Cr and C in the hard phases may result in uneven distribution in the microstructure, which increases the brittleness and eventually decreases toughness. Ceramic particles like tungsten carbide (WC) have reasonably good wettability with Fe–Cr and other Fe-based alloy powders [50]. Another important consideration that affects the mechanical properties is the presence of the eta phases in the composites. An increment in the hardness can be observed with the introduction of a Fe-Cr-based binder [51]. This increment is attributed to the hardness of WC-Co-based composites is affected by the eta phase. The higher the Eta phase content, the lower the binder phase proportion. The Eta phase is an intermetallic compound, and its hardness is significantly higher than that of the metal binder phase [52]. Therefore, the Eta phase is the dominant factor affecting the hardness of the samples with FeCr binder. However, the presence of an Eta phase affects the toughness of the material, as it is brittle and reduces the fracture toughness of the WC-based composite significantly.

3.4. Effect on the porosity

Porosity in the as-built can be observed in all the compositions of the WC-based composites fabricated with different laser process parameters. Process defects such as pores depend on the various factors that could occur during the fabrication process and lead to the formation of pores [53–55]. Powder morphology and rheology play an important role in the fabrication of the parts in this study the initial powder was used with wide variation in the particle size and mixed powder also showed a wide variation which in turn affects the porosity defect in the fabricated parts [56,57]. The characteristics of raw powder are considered to be a crucial factor affecting the microstructure and performance of the SLM-processed parts. The particle size distribution (PSD) of WC carbide produced through Selective Laser Melting (SLM) can vary depending on the specific process and materials used. The previous works show that the particle size of the powder batch and powder layer thickness used in SLM typically range from 45 to 120 μm and 50–150 μm, respectively [58]. However, the exact PSD can differ between studies, as some researchers have used WC powders with particle sizes ranging from microns to tens of microns [59]. A study by Zhao et al. fabricated WC-12Co cemented carbides through SLM and subsequent sintering, using a coarse-grained WC powder [60]. Another study by Bricín et al. focused on microstructural evolution in a WC-Co powder mixture during SLM and hot isostatic pressing, using a specific WC powder with an unspecified particle size distribution [61]. It’s important to note that the PSD of WC carbide can significantly impact the final properties of the manufactured parts, such as hardness, strength, and wear resistance. For instance, a narrower PSD can lead to better mechanical properties due to reduced porosity and increased density.

Porosity in Selective Laser Melting (SLM) can be influenced significantly by particle size distribution. A study shows that the porosity fraction and pore shape in SLM parts change depending on the melt pool size and shape, which is explained based on the local energy availability and particle size distribution [62,63]. Another study reveals that the porosity of laser-melted layers increases with the degree of size misfit between non-spherical and spherical powders [64]. Overall, it’s crucial to ensure a suitable particle size distribution for minimizing porosity in SLM-produced parts, as it seems to play a key role in the process. Porosity such as entrapped gas, and keyhole defect could be the reason to form due to this wide variation in the particle size.

It can be observed from Figs. 3–5 that the laser process parameters affect the porosity formation. Increasing the laser energy from 60 to 70 watts led to a reduction of the porosity in all the WC-based composites which can be explained by the following equation [65].

$$\eta_\nu = \frac{16}{15}\sqrt{\frac{m}{k\quad T}}\sigma \tag{2}$$

where η_ν denotes the liquid phase dynamic viscosity in the molten pool, m represents the atomic mass, k corresponds to the Boltzmann constant, T denotes the temperature of the melt pool, and σ denotes the surface tension. From the equation, it can be concluded that a specimen with lower laser power will have a lower melt pool temperature which leads to increases in the dynamic viscosity of the liquid phases in the melt pool and affects the spreadability and wettability of the powder particles and increases porosity/poor densification. Also, at lower energy density there might be a chance of unmelted particles which can affect the porosity formation in the as-built parts as in these areas powder particles may embank due to variation in the powder particles.

Increasing the laser energy decreases the viscosity of the melt pool and reduces the porosity due to better wettability and lower contact angle between the particles. As the laser energy increases, porosity can increase which can be caused by the WC grain coarsening, leading to balling effects during fabrication, and at higher energy densities, there is a greater possibility of evaporation and overheating at the melt pool, which can lead to the overall reduction of molten material from the melt pool, and porosity can form. Fig. 9. shows the volume percentage of the porosity present in the fabricated as-built parts. As explained before the reduction in the porosity can be noted by increasing the MLP (48–60 watts) while an increment of the MLP (60–72 watts) causes a further increment in the porosity. However, as for the porosity measurement, Image analysis has been performed by thresholding the image with a different threshold of greyscale, and during the porosity measurement, the cracks were also included as they share the same color threshold which could explain the high jump in porosity values at higher MLP (72 Watt).

3.5. Phase composition

Fig. 10 exhibits the XRD spectra of the WC-based cermet with different laser energy densities fabricated via SLM. The strongest peak of WC in all the fabricated parts can be observed. Besides WC, other diffraction peaks which were identified as M_3W_3C, α-Fe, W_xMC, and traces of W_2C $Cr_{0.3}W_{0.7}C_{0.5}$ also observed in the fabricated cermets. *α*–Fe diffractograms in the XRD analysis should be regarded as a solid solution of Fe-Cr. Fe is a weaker carbide former as compared to W and Cr but due to rich amount of the Fe-based binder in the WC-50Fe and WC-50FeCr led to the formation of the Fe-based carbide. In the case of the WC-20FeCr high intensity, WC and traces of W_2C diffraction peaks have been observed with the formation of W_xMC carbide. It could be noted that the α-Fe phase was absent in the cases of WC-20FeCr-based cermets due to the formation of the W_xMC by the interaction of the WC and Fe. Variations in the laser energy density and the changing weight percentage of the steel binder led to the introduction of the new intermetallic phases due to carbide and binder interaction.

Laser process parameters affect the formation of these metallic carbides based on the W and Fe due to changes in the overall melt pool

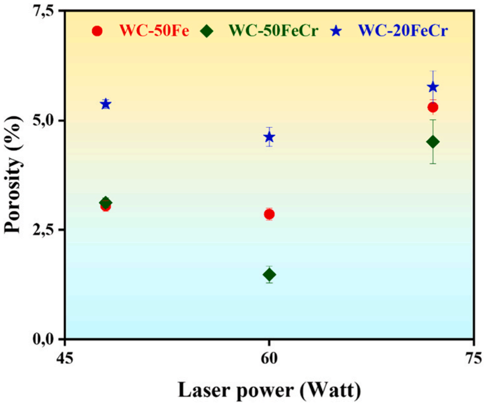

Fig. 9. Porosity micrograph of the WC-based composites fabricated via SLM.

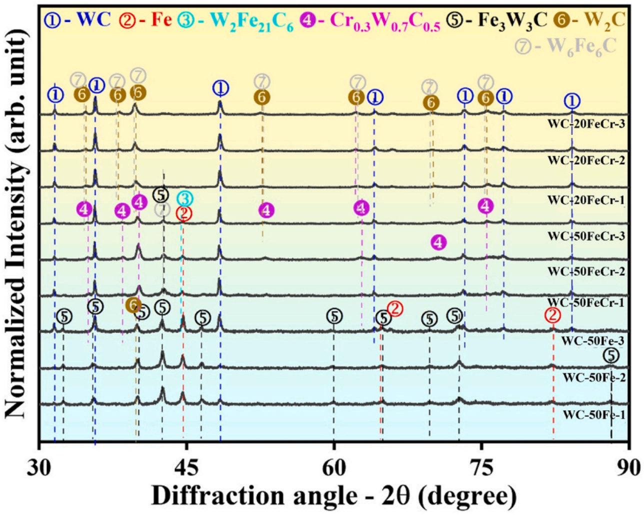

Fig. 10. XRD pattern of the WC-based cermets fabricated via SLM with different laser power.

temperature. The effect of the laser energy density led to the change in the microstructure due to which slight variation in the intensity of the diffraction peak of the WC and intermetallic phase can be observed. To support the formation of the different WC and intermetallic phases, Energy Dispersive Spectroscopy (EDS) point analysis has been performed and depicted in Fig. 11 conforming the formation of different intermetallic carbides with different laser process parameters which corroborates with the XRD data. Adaption of various Fe-based binders with different percentages led to the formation of such intermetallic carbides. Moreover, the adapted laser process parameter also plays a significant role in such occurrence of reaction. Increasing the laser peak power generally increases the melt pool temperature and increases a significant duration to cause such intermetallic reactions and form such intermetallic carbides. In Fig. 11 (a), it can be observed that all the spectra exhibit a variation in the carbon ratio at different WC particles. This variation could be attributed to the carbon reaction with Fe and W to form intermetallic carbide. The introduction of FeCr-based binders with different percentages leads to the formation of these intermetallic carbides. In Fig. 11(b) variation in the composition of the element can be observed at different regions of the microstructure suggesting the formation of the various intermetallic carbides as depicted in XRD data. Similarly in Fig. 11 (c), the variation of element percentage can be observed suggesting the formation of such complex intermetallic carbides.

4. Conclusion

WC-Fe and FeCr-based composites with different weight percentages of the metallic binder were fabricated successfully through a Selective laser melting process utilizing a unique Laser beam modulation technique. The microstructure and phase analysis of the fabricated parts were conducted and led to the following conclusions.

1. Laser beam optimization helps to control the melt pool temperature by preheating and extending cooling time which controls the sudden thermal gradient and reduces the thermal residual stress and is seen as a possible solution to fabricate the cermets parts with a reduction in the process induce defects such as major cracks.
2. Modulation of laser beam profiles is accomplished by varying laser peak power (48, 60, and 72 watts) with constant laser exposure time

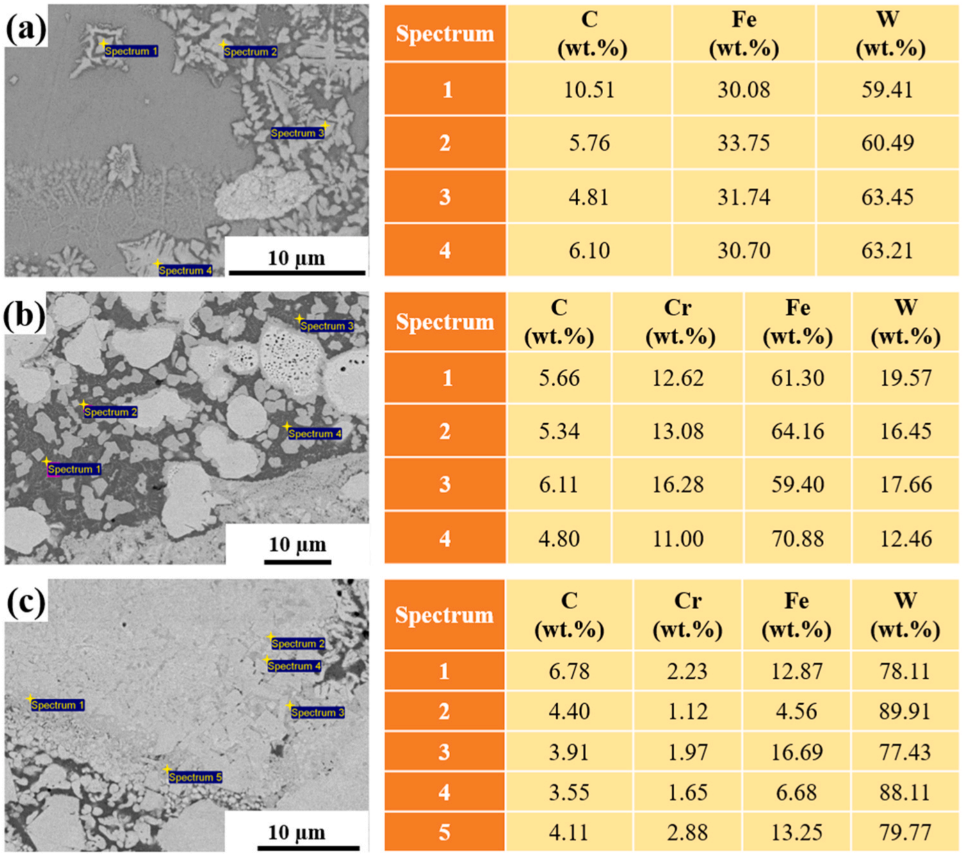

Spectrum	C (wt.%)	Fe (wt.%)	W (wt.%)
1	10.51	30.08	59.41
2	5.76	33.75	60.49
3	4.81	31.74	63.45
4	6.10	30.70	63.21

Spectrum	C (wt.%)	Cr (wt.%)	Fe (wt.%)	W (wt.%)
1	5.66	12.62	61.30	19.57
2	5.34	13.08	64.16	16.45
3	6.11	16.28	59.40	17.66
4	4.80	11.00	70.88	12.46

Spectrum	C (wt.%)	Cr (wt.%)	Fe (wt.%)	W (wt.%)
1	6.78	2.23	12.87	78.11
2	4.40	1.12	4.56	89.91
3	3.91	1.97	16.69	77.43
4	3.55	1.65	6.68	88.11
5	4.11	2.88	13.25	79.77

Fig. 11. Energy Dispersive Spectroscopy point analysis of the SLM processed WC-FeCr based composites fabricated with different Fe-based binders (a) WC-50Fe-2, (b) WC-50FeCr-2, (c) WC-20FeCr-2.

for each laser beam profile. The adaptation of the different laser beam profiles for WC-based composites with different compositions of Fe-based binder led to the evolution in the microstructure and phase formation.

3. The microstructure of the SLM-ed parts indicates that higher laser energy density reduces heterogeneity and porosity. However, maximum energy density resulted in higher melt pool temperature and coarse microstructure which introduces more process defects. The as-built parts display the dual-phase microstructure with coarser and finer WC grains.
4. Phase analysis revealed the formation of the secondary tungsten carbide and intermetallic carbide at higher energy density due to slower heating and cooling rate which led to the evolution of the carbon and form of a complex intermetallic carbide.
5. Mechanical properties such as microhardness are affected by the porosity, dual-phase WC, and composition of the WC in the as-parts. An increment in the hardness can be observed by increasing the WC percentage in the FeCr binder. The maximum microhardness has been achieved for the WC-20 wt% FeCr i.e., 2049 ± 209 HV_1.

It can be concluded the fabrication of the WC-based composites by modulation of the laser beam could be a possible solution for fabricating these brittle materials. However, fabricating parts without process defects is a challenge and requires further research to obtain the final parts with improved microstructure and mechanical properties.

Ethical approval

Not applicable.

Supplementary information

Not Applicable.

Funding

This work was supported by Estonian Research Council grant no. PRG1145 “Composites ‘ceramic-Fe-alloy’ for a wide range of application conditions”.

Declaration of Competing Interest

The authors declare that they have no known competing financial interests or personal relationships that could have appeared to influence the work reported in this paper.

Data availability

The present data forms a part of the ongoing study, and the results may be shared upon reasonable request from the corresponding author (s).

References

[1] R.S. Khmyrov, V.A. Safronov, A.V. Gusarov, Procedia IUTAM 23 (2017) 114.
[2] J. Liu, J. Chen, L. Zhou, B. Liu, Y. Lu, S. Wu, X. Deng, Z. Lu, Z. Xie, W. Liu, J. Liu, Z. Qu, Acta Metall. Sin. (Engl. Lett.) 34 (2021) 1245.
[3] D. Zhang, C. Kenel, D.C. Dunand, Acta Mater. 221 (2021) 117420.
[4] Z.Z. Fang, M.C. Koopman, and H. Wang, in edited by V.K.B.T.-C.H.M. Sarin (Elsevier, Oxford, 2014), pp. 123–137.
[5] J. Tarraste M.; Kolnes, M.; Kübarsepp, J.; Juhani, K.; Viljus, M.; Külaviir, in *Euro PM2020 Congress Proceedings* (2020).
[6] E. Molobi, N. Sacks, M. Theron, Addit. Manuf. Lett. 2 (2022) 100028.
[7] M. Tarraste, J. Kübarsepp, K. Juhani, A. Mere, M. Kolnes, M. Viljus, B. Maaten, Int J. Refract Met. Hard Mater. 73 (2018) 183.
[8] H. Li, H. Zhang, G. Li, D. Zhao, Z. Jiang, Int J. Refract Met. Hard Mater. 108 (2022) 105951.
[9] J. Kübarsepp, K. Juhani, Int. J. Refract Met. Hard. Mater. 92 (2020) 105290.
[10] 2020 (2020).
[11] H.S. Maurya, J. Jayaraj, Z. Wang, K. Juhani, F. Sergejev, K.G. Prashanth, J. Alloy. Compd. 959 (2023) 170496.
[12] R. Kumar, A. Kariminejad, M. Antonov, D. Goljandin, P. Klimczyk, I. Hussainova, Sustainability 15 (2023).
[13] M. Tarraste, J. Kübarsepp, K. Juhani, A. Mere, M. Kolnes, M. Viljus, B. Maaten, Int. J. Refract Met. Hard. Mater. 73 (2018) 183.
[14] R. Kumar, M. Antonov, U. Beste, D. Goljandin, Int. J. Refract Met. Hard. Mater. 86 (2020) 105126.
[15] A. Aramian, S.M.J. Razavi, Z. Sadeghian, F. Berto, Addit. Manuf. 33 (2020) 101130.
[16] Y. Yang, C. Zhang, D. Wang, L. Nie, D. Wellmann, Y. Tian, Int. J. Adv. Manuf. Technol. 108 (2020) 1653.
[17] X. Shi, H. Yang, G. Shao, X. Duan, S. Wang, Ceram. Int 34 (2008) 2043.
[18] A. Aramian, Z. Sadeghian, D. Wan, Y. Holovenko, S.M.J. Razavi, F. Berto, Mater. Charact. 178 (2021) 111289.
[19] C. Zhao, Z. Wang, D. Li, L. Kollo, Z. Luo, W. Zhang, K.G. Prashanth, J. Mater. Res. Technol. 9 (2020) 13097.
[20] S. Son, J.M. Park, S.H. Park, J.-H. Yu, H. Kwon, H.S. Kim, Mater. Lett. 293 (2021) 129683.
[21] X. Li, Y. Zhao, Z. Guo, Y.Y. Liu, H. Wang, J. Zhang, D. Yi, Y. Cao, X. Yang, B. Liu, Y. Y. Liu, P. Bai, Int. J. Refract Met. Hard. Mater. 104 (2022) 105787.
[22] M. Xing, H. Wang, Z. Zhao, Y. Zhang, H. Lou, C. Liu, M. Wang, X. Song, Ceram. Int (2022).
[23] R. Kumar, I. Hussainova, M. Antonov, H.S. Maurya, M. Rodríguez Ripoll, Wear 552–553 (2024).
[24] C. Zhao, Z. Wang, D. Li, L. Kollo, Z. Luo, W. Zhang, K.G. Prashanth, Int. J. Plast. 138 (2021) 102926.
[25] H.S. Maurya, L. Kollo, M. Tarraste, K. Juhani, F. Sergejev, K.G. Prashanth, Trans. Indian Inst. Met. (2022).
[26] P. Mercelis, J.P. Kruth, Rapid Prototyp. J. 12 (2006) 254.
[27] T. Mukherjee, W. Zhang, T. DebRoy, Comput. Mater. Sci. 126 (2017) 360.
[28] P. Peralta, R. Dickerson, J.R. Michael, K.J. McClellan, F. Chu, T.E. Mitchell, Mater. Sci. Eng. A 261 (1999) 261.
[29] K.G. Prashanth, H. Shakur Shahabi, H. Attar, V.C. Srivastava, N. Ellendt, V. Uhlenwinkel, J. Eckert, S. Scudino, Addit. Manuf. 6 (2015) 1.
[30] P. Ma, P. Ji, Y. Jia, X. Shi, Z. Yu, K.G. Prashanth, Materials 14 (2021) 330.
[31] P. Ma, Y. Jia, K.G. Prashanth, S. Scudino, Z. Yu, J. Eckert, J. Alloy. Compd. 657 (2016) 430.
[32] A. Sadhu, A. Choudhary, S. Sarkar, A.M. Nair, P. Nayak, S.D. Pawar, G. Muvvala, S. K. Pal, A.K. Nath, Surf. Coat. Technol. 389 (2020) 125646.
[33] J.M. Amado, M.J. Tobar, A. Yáñez, V. Amigó, J.J. Candel, Phys. Procedia 12 (2011) 338.
[34] Z. Chen, Y. Xiang, Z. Wei, P. Wei, B. Lu, L. Zhang, J. Du, Appl. Phys. A Mater. Sci. Process 124 (2018) 1.
[35] B. Liu, G. Fang, L. Lei, Appl. Math. Model 92 (2021) 505.
[36] W. Li, S. Li, J. Liu, A. Zhang, Y. Zhou, Q. Wei, C. Yan, Y. Shi, Mater. Sci. Eng. A 663 (2016) 116.
[37] A. Aramian, Int. J. Refract. Met. Hard. Mater. 87 (2020) 105171.
[38] H.S. Maurya, L. Kollo, M. Tarraste, K. Juhani, F. Sergejev, K.G. Prashanth, 3, D. Print. Addit. Manuf. 10 (2021) 640.
[39] F. Trevisan, F. Calignano, M. Lorusso, J. Pakkanen, A. Aversa, E.P. Ambrosio, M. Lombardi, P. Fino, D. Manfredi, Materials 10 (2017).
[40] H.S. Maurya, R.J. Vikram, K. Kosiba, K. Juhani, F. Sergejev, S. Suwas, K. G. Prashanth, J. Alloy. Compd. 938 (2023) 168416.
[41] P.A. Hooper, Addit. Manuf. 22 (2018) 548.
[42] J. Zeisig, N. Schädlich, J. Hufenbach, H. Wendrock, J. Kimme, U. Kühn, J. Alloy. Compd. 816 (2020) 152544.
[43] S. Cao, Z. Chen, C.V.S. Lim, K. Yang, Q. Jia, T. Jarvis, D. Tomus, X. Wu, JOM 69 (2017) 2684.
[44] S. Da Sun, D. Fabijanic, C. Barr, Q. Liu, K. Walker, N. Matthews, N. Orchowski, M. Easton, M. Brandt, Surf. Coat. Technol. 333 (2018) 210.
[45] H.S. Maurya, K. Juhani, M. Viljus, F. Sergejev, J. Kübarsepp, Ceram. Int 50 (2024) 8695.
[46] R. Rahimi, O. Volkova, H. Biermann, J. Mola, Adv. Eng. Mater. 21 (2019).
[47] S. Ma, J. Xing, Y. He, Y. Li, Z. Huang, G. Liu, Q. Geng, Mater. Chem. Phys. 161 (2015) 65.
[48] H. Tian, M. Zhang, Y. Peng, Y. Du, P. Zhou, Int. J. Refract. Met. Hard. Mater. 78 (2019) 240.
[49] C. Yin, Y. Peng, J. Ruan, L. Zhao, R. Zhang, Y. Du, Materials 14 (2021).
[50] R. Yuan, X. Bai, H. Li, Z. Zhang, S. Sun, Y. Zhai, Mater. Res. Express 8 (2021).
[51] J. Heinrichs, S. Norgren, S. Jacobson, K. Yvell, M. Olsson, Int. J. Refract. Met. Hard. Mater. 85 (2019) 105035.
[52] X. Li, J. Zhang, Q. Zhang, X. Zhang, V. Ji, J. Liu, Coatings 13 (2023).
[53] Z. Zhao, C. Dong, D. Kong, L. Wang, X. Ni, L. Zhang, W. Wu, L. Zhu, X. Li, Mater. Charact. 182 (2021) 111514.
[54] W. Chen, C. Chen, X. Zi, X. Cheng, X. Zhang, Y.C. Lin, K. Zhou, Mater. Sci. Eng.: A 726 (2018) 240.
[55] P.A. Hooper, Addit. Manuf. 22 (2018) 548.
[56] L. Zhang, C. Hu, Y. Yang, R.D.K. Misra, K. Kondoh, Y. Lu, Addit. Manuf. 55 (2022) 102820.
[57] D. Bricin, A. Kriz, MM Sci. J. 2019 (2019) 2939.
[58] C. Chen, B. Huang, Z. Liu, Y. Li, D. Zou, T. Liu, Y. Chang, L. Chen, Addit. Manuf. 63 (2023) 103410.
[59] N. Ku, J.J. Pittari, S. Kilczewski, A. Kudzal, JOM 71 (2019) 1535.
[60] Y. Zhao, H. Wang, L. Zhang, X. Li, Z. Guo, J. Zhang, D. Yi, B. Liu, P. Bai, J. Mater. Res. Technol. 20 (2022) 3512.

[61] D. Bricín, M. Ackermann, Z. Jansa, D. Kubátová, A. Kříž, Z. Špirit, J. Šafka, Met. (Basel) 10 (2020) 1.

[62] P. Kumar, J. Farah, J. Akram, C. Teng, J. Ginn, M. Misra, Int. J. Adv. Manuf. Technol. 103 (2019) 1497.

[63] Z. Wu, M. Asherloo, R. Jiang, M.H. Delpazir, N. Sivakumar, M. Paliwal, J. Capone, B. Gould, A. Rollett, A. Mostafaei, Addit. Manuf. 47 (2021) 102323.

[64] T.J. Jeon, T.W. Hwang, H.J. Yun, C.J. VanTyne, Y.H. Moon, Appl. Sci. (Switz.) 8 (2018).

[65] D. Liu, W. Yue, J. Kang, C. Wang, Materials 14 (2021).